

pubs.acs.org/journal/ascecg Research Article

Investigation of the Degradation Phenomena of a Proton Exchange Membrane Electrolyzer Stack by Successive Replacement of Aged **Components in Single Cells**

Benjamin Kimmel, Tobias Morawietz, Indro Biswas, Noriko Sata, Pawel Gazdzicki, Aldo Saul Gago,* and Kaspar Andreas Friedrich



Cite This: ACS Sustainable Chem. Eng. 2025, 13, 4330–4340



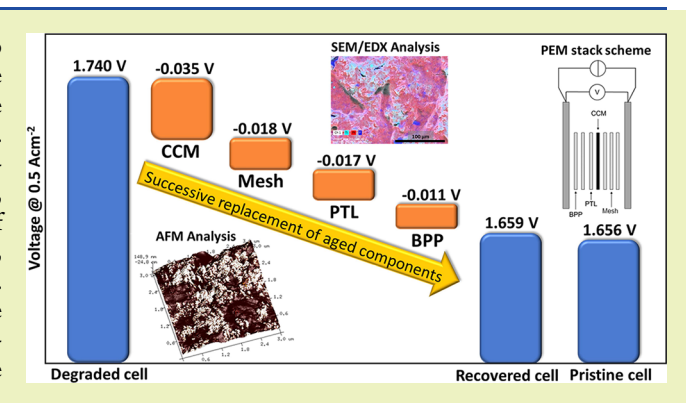
ACCESS I

III Metrics & More

Article Recommendations

Supporting Information

ABSTRACT: Due to their compactness and high flexibility to operate under dynamic conditions, proton exchange membrane water electrolyzers (PEMWEs) are ideal systems for the production of green hydrogen from renewable energy sources. For the widespread implementation of PEMWEs, an understanding of their degradation mechanism is crucial. In this work, we analyze a commercial PEMWE stack via a novel approach of breaking down from the stack to the single-cell level. Therefore, the disassembled stack components are cut to fit into single cells. Then, the aged components are successively replaced with pristine or regenerated components (cleaned and polished), and electrochemical characterizations are conducted to investigate the contributions of the individual components on performance losses.



In addition, several underlying degradation phenomena are identified using different physical ex-situ analysis methods. The catalystcoated membrane (CCM) contributes the most to performance degradation because of contamination and ionomer rearrangement. Additionally, traces of calcium, likely due to insufficient water purification used during operation or for cleaning the cell components, were found. Significant oxidation was observed on the anodic components, while the electronic conductivity on the cathode side remained unchanged. The combination of electrochemical characterization with stepwise regeneration processes and physical ex-situ analysis allows to draw conclusions about the impact of different components on degradation and to analyze the underlying aging mechanisms occurring in each component.

KEYWORDS: PEM electrolysis, degradation, electrochemical analysis, successive regeneration, commercial stack

1. INTRODUCTION

The widespread implementation of renewable energy technologies is a pressing challenge for our society, requiring not only the reduction of anthropogenic CO₂ emissions, which are among the major greenhouse gases but also the reduction of the dependence on fossil fuels. The increasing weather anomalies highlight the importance of shifting from fossil fuels to renewable energy sources, necessitating the expansion of the share of renewable energy generation. However, due to weather-dependent fluctuations in renewable energy generation, for example, wind and solar energy, the resilience of the electrical grid must be improved through large-scale energy storage. Therefore, hydrogen, as a secondary energy carrier, may play a key role in the future as a chemical energy source.² Green hydrogen production by water electrolysis to decouple energy production and demand is a highly promising approach for grid balancing while maintaining high overall energy production efficiency. Furthermore, hydrogen can be transported and thus represents a good opportunity for connecting

regions or countries with high potential for renewable energy generation and regions with limited renewable energy potential.2 Due to their rapid response time and wide operational range, proton exchange membrane water electrolyzer (PEMWE) systems are highly suitable for coupling with renewable energy technologies.^{3,4} Furthermore, PEMWE systems can reach high efficiency and high power density while maintaining a compact design and outstanding gas quality.3,5,6 However, in addition to maintaining high efficiency, ensuring a long lifetime is a pressing challenge. The lifetime of a PEMWE is dominated mainly by the degradation of the stack. Therefore, the development of robust

Received: September 4, 2024 Revised: February 21, 2025 Accepted: February 24, 2025 Published: March 7, 2025





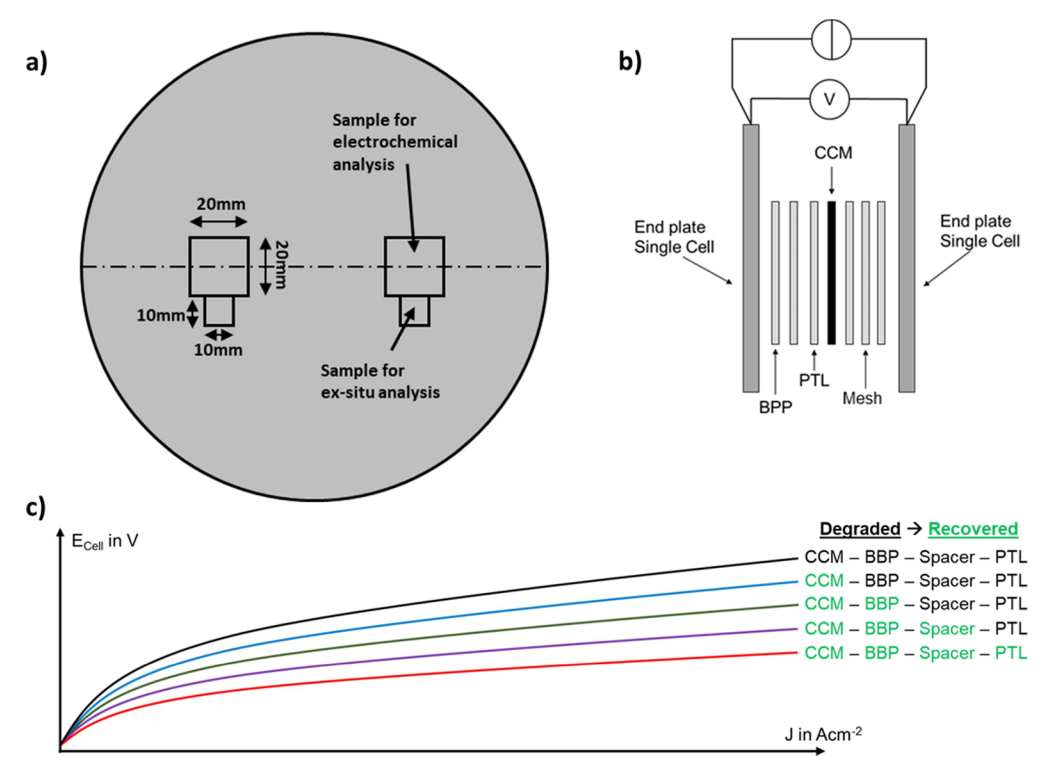


Figure 1. Scheme of stepwise recovery: (a) Position and size of the samples cut out of the stack components. (b) Scheme of a single cell and (c) expected performance improvement due to the stepwise recovery process of the stack samples.

and stable yet cost-effective stack components has received intense attention. The main stack components are as follows: the membranes, which separate the anode and cathode, mostly consist of a proton-conducting perfluorosulfonic acid and are often directly coated with the catalyst material to form the catalyst coated membrane (CCM). In direct contact with the CCMs are the porous transport layers (PTLs), which are responsible for water and gas management, followed by bipolar plates (BPPs), which separate the cells in the stack while maintaining good electrical conductivity. Different approaches are present for water management, e.g., the use of integrated flow fields in BPP, 8,9 additional components such as titanium meshes between the BPP and the PTLs and PTLs with pore size gradients starting from a mesh-like structure and ending in a microporous layer (MPL). 10,111 The dominant degradation phenomena are different for each component because of the different materials and operating conditions and must be analyzed and investigated separately. Numerous studies have been conducted on the durability and degradation effects of PEMWE, with a strong focus on the catalytic layers 11-27 but also on the degradation of membranes, ^{17,28,29} PTLs^{11,13,18,26,30,31} and BPPs. ^{26,32,33} Feng et al. summarized the reports on degradation and discussed the origin of degradation for the individual components.³⁴ The main degradation phenomena of PEMWE include structural changes in the catalyst layer, contamination due to impurities in the feedwater, and corrosion and passivation of the titanium components, namely, PTLs and BPPs.²⁶ However, the effects of different components on the performance losses are still not fully understood.

For commercial PEMWE stacks, the detailed operation histories are often unknown, but degradation phenomena remain to be investigated for further improvement with regard to cost, performance and durability. Therefore, this study

considers the approach of breaking down from a stack to a single cell using a commercial 250 cm² PEMWE stack with unknown operation conditions. The degradation phenomena were analyzed using electrochemical characterization methods and physical ex situ analysis.

Degradation studies have usually been conducted under well-defined and various operation conditions and have focused on overall performance losses. While partially ex situ methods were used to analyze the degradation phenomena of the different components, the impact on the performance loss for each component could not be determined. By breaking down from the stack to a single cell and replacing and recovering components individually in this study, it was possible to identify the causes of degradation, analyze the underlying phenomena and quantify the impact of the various components on the overall performance.

2. EXPERIMENTAL SECTION

2.1. Methodology. An aged commercial 6-cell short stack with a circular active area of 250 cm² from an undisclosed company was characterized electrochemically using an in-house build test bench designed for 10 kW power. The specific operation history of the stack is unknown, but the operation time is expected to be approximately 10,000 h. To ensure good water management in the stack, titanium mesh is used as the flow field. In this case, the BPPs are plain titanium plates. The PTL is made of sintered titanium, which connects the CCM and the mesh electrically and simultaneously ensures good gas removal. After receiving the operated short stack, electrochemical characterization was carried out through the measurement of a polarization curve, short-term operation, and electrochemical impedance spectroscopy (EIS) measurements using a setup capable of measuring up to 600 A and up to 10 cells in parallel. In this setup, the "Impedance Spectrum Analyser IM6" and the "dynamic electronic load EL1000" by Zahner-Elektrik GmbH & Co. KG³⁵ were used. In addition, the power supply of the in-house test bench was connected as shown in the scheme in the Supporting Information (SI) in Figure

S1. The dynamic load, controlled by the ThalesXT software,³⁵ periodically consumes a portion of the current provided by the power supply according to a predefined amplitude and frequency and thus operates as an EIS device. This setup was used to carry out measurements at different current densities ranging from 25 to 250 A with amplitudes between 4 and 20 A. The polarization curve was recorded according to the protocol established by the Joint Research Centre (JRC)³⁶ using script control of the in-house build test bench.

The stack was subsequently disassembled to investigate the impact and degradation phenomena of the different components through single cell measurements and physical ex-situ analysis. For this study, components from two different positions of cell 6 were selected for analysis. The samples were cut out of the stack components, as shown in Figure 1a. To leave the samples unaffected during preparation, the stack components were covered with films, firmly clamped and cut with hand lever scissors; this enabled preparation of the samples without any chipping and without the use of cooling liquids. The sample sizes were 20×20 and 10×10 mm² for single cell measurements and for ex-situ analysis, respectively.

The prepared stack components were placed between the end plates of the single cell, as shown in the scheme of Figure 1b. To quantify the impact on the performance losses separately, the aged components were replaced or recovered stepwise as specified in Table 1.

Table 1. State of the Components for Each Regeneration Step

Step	CCM	Mesh	PTL	BPP
1	Degraded	Degraded	Degraded	Degraded
2	Pristine	Degraded	Degraded	Degraded
3	Pristine	Regenerated	Degraded	Degraded
4	Pristine	Regenerated	Regenerated	Degraded
5	Pristine	Regenerated	Regenerated	Regenerated
R	Pristine	Pristine	Pristine	Pristine

First, the used CCM was replaced with a pristine CCM, while the other components remained unchanged. Because the catalytic layer is very sensitive to disassembly and assembly processes, the CCM was the first component to be replaced and was replaced again when the adjacent PTLs were recovered. This procedure was repeated for each component until obtaining a fully recovered single cell. It was anticipated that an increase in performance would be observed, with varying degrees of improvement for each component, as illustrated in the scheme presented in Figure 1c.

For the recovery steps, the CCM was replaced with a pristine CCM, while the Ti components were regenerated by removing the ${\rm TiO_x}$ layer using sandpaper with increasingly smaller grain sizes starting with P1000 and ending with P5000. The regenerated Ti components were subsequently cleaned in an ultrasonic bath. The samples were first immersed in isopropanol for 30 min in an ultrasonic bath and then in deionized (DI) water. Based on this series of experiments, conclusions can be drawn about the quantitative impact of the individual components on degradation.

2.2. Data Correction. The membrane used in the stack has a thickness of approximately 300 μ m, which is approximately three times higher than the typical thickness of state-of-the-art membranes and is not commercially available anymore. By contrast, membranes with a thickness of approximately 50 μ m have shown very promising results in previous studies, ^{37–39} however, membranes with thicknesses >100 μ m are more widely used. Consequently, as the pristine CCM used for stepwise recovery in single cell measurements, a commercial 120- μ m-thick membrane was chosen. The loading used along with the 120- μ m-thick commercial membrane was approximately 2.5 mg cm⁻², whereas the loading used with the 300- μ m-thick membrane is unknown. Nevertheless, it is highly likely that the loading is in fact higher. As demonstrated by Rozain et al., Ir loadings exceeding approximately 0.5 mg cm⁻² have minimal impact on the perform-

ance. We consequently, it is reasonable to conclude that the primary impact of the substitution of the thicker CCM by the thinner CCM utilized for stepwise recovery is the change in the ohmic resistance. To evaluate the performance improvement of step 2 in Table 1, the reduction in the ohmic resistance must be considered. Accordingly, the performance of the degraded stack (cell 6), corresponding to Step 1 in Table 1, was adjusted to account for the reduction in the associated ohmic resistance when the 300- μ m-thick membrane is changed to the 120- μ m-thick membrane. This reduction was calculated based on experimental results. Therefore, the initial stack voltage U_{Initial} measured by the manufacturer after assembly, was subtracted from the measured voltage $U_{120\mu\text{m}}$ using a pristine cell including the commercial 120 μ m membrane. This leads to a decrease in the ohmic resistance obtained according to

Equation 1:

$$\Delta\Omega(i) = \frac{\Delta U}{i} = \frac{\left(U_{\text{Initial}} - U_{120\mu\text{m}}\right)}{i}$$
 (1)

Here, $\Delta\Omega(i)$ is the current-dependent decrease in the ohmic resistance at the corresponding current density i. The polarization curve $U_{\rm degraded}(i)$ using the CCM with a 300- μ m-thick membrane was corrected by the ohmic resistance according to eq 2 to make steps 1 and 2 comparable:

$$U_{\text{corr}}(i) = U_{\text{degraded}}(i) - \Delta\Omega(i) \times i$$
 (2)

In the following, $U_{\rm corr}(i)$ serves as the baseline to evaluate the recovery steps. Additionally, this calculation can be used to determine the change in ohmic resistance to scale the EIS measurements accordingly. Figure S2 in the SI compares the uncorrected and corrected polarization curves considering the reduction in ohmic resistances when going from a 300- μ m-thick to a 120- μ m-thick membrane calculated using eq 2 to determine the voltage for each current density step. The slightly higher performance in the low-current region of the degraded curve in Figure S2 can presumably be attributed to smaller deviations in the experimental results used for the calculation. In the following, degraded performance always refers to the aged stack and is corrected as specified.

2.3. Physical Characterization. To investigate the underlying degradation mechanisms, the $10 \times 10 \text{ mm}^2$ samples were analyzed using the following physical ex situ methods.

2.3.1. X-ray Diffraction. X-ray diffraction (XRD) was performed using a D8 ADVANCE instrument (Bruker AXS GmbH, Germany) to analyze the phases in the cell specimens. A parallelized Cu K α X-ray source was used as the incident beam ($\lambda=1.54178$ Å, 40 kV–40 mA). An equatorial soller slit (0.41°) was used with a LYNXEYE XET detector operated in 0D high-energy-resolution mode to record diffractograms by $2\theta\!-\!\theta$ scan. Grazing incidence X-ray diffraction (GIXRD) at different incident angles starting from 1° was used to analyze the CCM of the commercial stack.

2.3.2. Atomic Force Microscopy. The surface structures and electronic conductivities of the CCM, PTLs, BPPs and meshes were analyzed using an Icon XR atomic force microscope (AFM) (Bruker, Karlsruhe) equipped with a PF-TUNA amplifier module. The AFM was operated in the PF-TUNA mode to simultaneously measure the force—separation curves and the electronic conductivity. In addition, the DCUBE-TUNA mode with a hold time of 100 ms and a ramp from 0 to 3 V with 128×128 Pixels for $3 \, \mu \text{m}^2$ was used with DDESP diamond-coated conductive tips (Nanosensors).

2.3.3. X-ray Photoelectron Spectroscopy. The chemical composition of the surfaces was analyzed by X-ray photoelectron spectroscopy (XPS). The measurements were carried out on a spectrometer with a hemispherical electron analyzer and a base pressure of 2 \times 10 $^{-10}$ mbar (ThermoScientific/FEI ESCALAB Xi $^{+}$) using monochromatized Al K α radiation with an energy of 1486.7 eV. The energy axis was calibrated using the Ag 3d signal of an ion-etched silver sample as a reference. Signal fitting for quantification and detailed analyses was carried out using convoluted Gaussian/Lorentzian peak profiles. 41 The samples, particularly the CCM, PTLs, BPPs and contact meshes, were clamped to stainless steel sample holders.

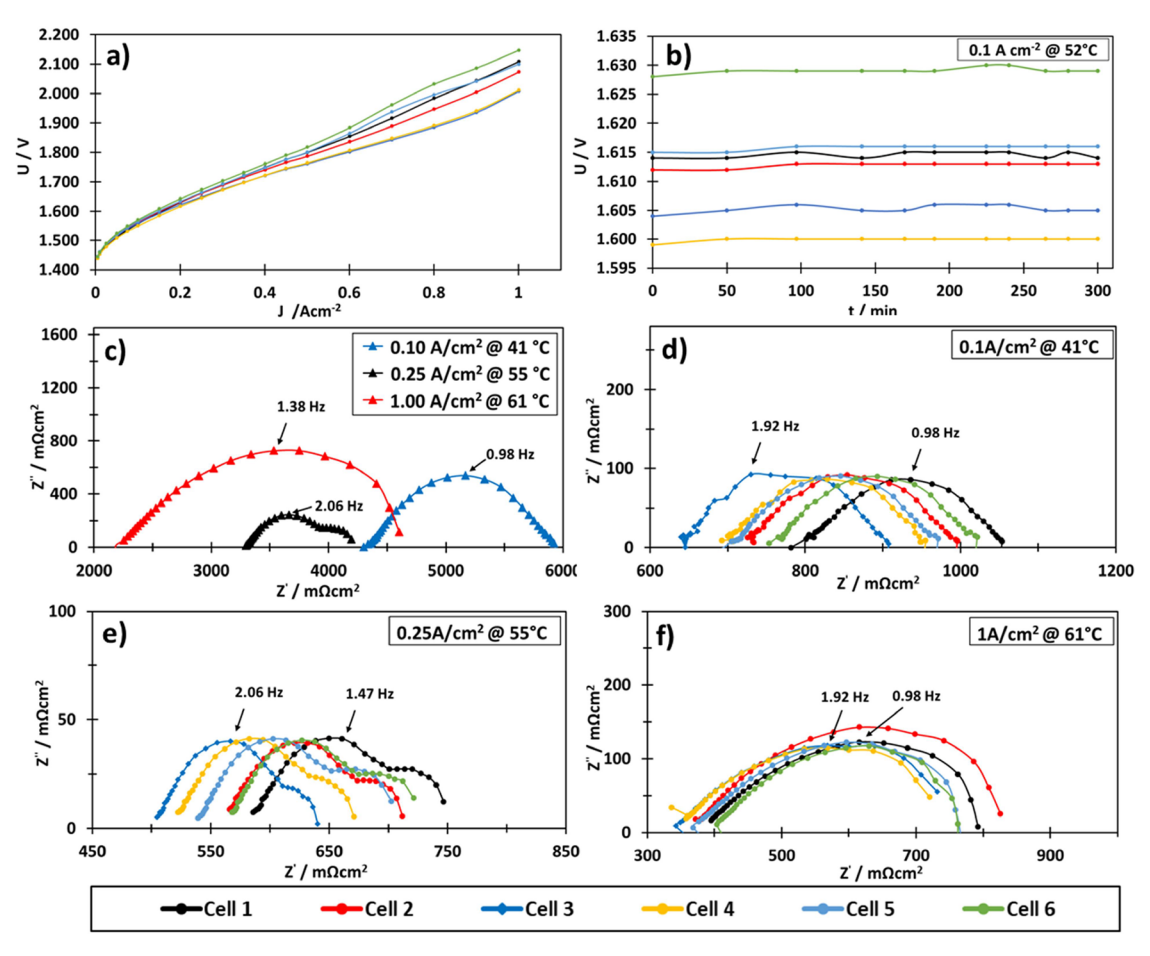


Figure 2. Electrochemical analysis of the aged stack: (a) polarization curve of the individual cells (not corrected), (b) short-term operation of the individual cells, (c) impedance measurement in Nyquist representation of the whole stack analyzed at 0.1, 0.25, and 1.0 A cm⁻², (d) impedance measurement in Nyquist representation of the individual cells analyzed at 0.1 A cm⁻², (e) 0.25 A cm⁻² and (f) 1.0 A cm⁻². The plotted frequency ranges start from 300 to 400 Hz and end at 3–100 m Hz, depending on the current density.

2.3.4. Scanning Electron Microscope/Energy Dispersive X-ray System. The scanning electron microscope (SEM) used in this study was a JEOL field emission microscope JSM-7200F with a Schottky emitter at 10⁻⁴ Pa vacuum. Secondary electron images were taken by Everhard—Thornley—SE-detector. The analysis conditions, such as the accelerating voltage, detector and measurement mode, are given for each image. The samples (CCMs, PTLs, BPPs, meshes) were glued with double-sided conductive tape to a large sample holder and measured successively. A Quantax XFlash6/60 (Bruker Nano GmbH) was used for energy dispersive X-ray measurements (EDX).

3. RESULTS AND DISCUSSION

The inspection of the commercial 6-cell short stack with an unknown operation history was carried out as follows:

- 1. Electrochemical characterization of the stack: including polarization curves, EIS and short-term operation.
- 2. Sample cut from the stack for testing in single cell and component regeneration.
- Sample cut from the stack for physical characterization: AFM, XPS, SEM/EDX, and XRD.
- **3.1. Electrochemical Analysis.** First, the degraded stack was characterized prior to starting the disassembly and stepwise recovery process.
- 3.1.1. Stack Characterization. By comparing the polarization curve of the received stack and the curve measured at the beginning of life (BOL) by the manufacturer, a pronounced degradation of 0.88~V at $1~A~cm^{-2}$ of the stack

was confirmed. The corresponding curves are provided in SI Figure S3.

Figure 2a shows the uncorrected polarization curves of each individual cell of the aged stack. Deviations between the cells increase at higher current densities. A short-term operation of approximately 5 h was conducted to verify the behavior of the cells. The corresponding plot is shown in (b). The current density was kept low at 0.1 A cm⁻² to avoid high potentials and temperatures and thus prevent additional degradation.

Figure 2c shows the results of the uncorrected EIS measurements of the aged stack represented as Nyquist plots for 0.10, 0.25, and 1.00 A $\rm cm^{-2}$.

The high frequency resistance (HFR), which corresponds to the ohmic resistance of the cell, is determined by the first intersection with the *x*-axis. With increasing current density, the HFR decreases. The large change in the HFR can be explained by the temperature difference caused by the changes in the heat production of the stack. In particular, below 65 °C, temperature strongly affects the resistance and performance. When operating at low current densities, the heat generation of the stack is much lower than that at higher current densities. Thus, the operating temperature at 0.10 A cm⁻² was 41 °C, whereas at 0.25 and 1.00 A cm⁻², it increased to 55 and 61 °C, respectively. This trend can also be observed for the different cells of the stack, as displayed in Figure 2d–f. In addition, small differences were measured between cells following a

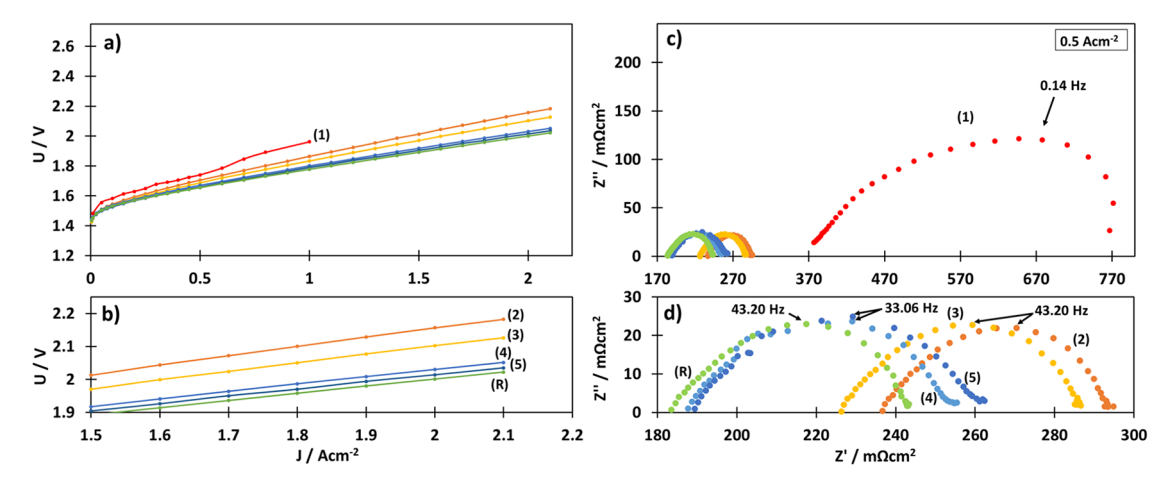


Figure 3. (a) Progression of the polarization curves through the step-by-step regeneration of the individual components, starting with all-degraded components and ending with the fully refreshed cell. (b) Magnification of the current density range of 1.5-2.2 A cm⁻². (c) Progression of the electrochemical impedance spectroscopy measurements. (d) Higher-magnification image for better differentiation in the range of 180-300 m Ω cm². The plotted frequency ranges start from 10 kHz and end at 20-100 mHz for the single cell, and from 180 Hz to 10 mHz for the degraded stack samples, showing positive Z'' values in the negative Nyquist plots. For (1), data corrected as described in Section 2.2 are used. The labels correspond to Table 1.

consistent behavior. The cells in the center of the stack, namely, cell 3 and cell 4, have the lowest resistances. Furthermore, from the center to the end plates, the resistance increases across cell 2 and cell 5 and is the highest at cells 1 and 6. This phenomenon can be explained by temperature differences within the stack. Strongest heat dissipation occurs at the end plates of the stack; therefore, we assume that a temperature gradient exists along the stack with higher temperatures in the center and lower temperatures at the end plates. This assumption is in good agreement with the measured data, where a clear trend in the HFR according to the cell position and current density was measured. The data are provided in SI Table S1.

Interestingly, the overall resistance first decreases from 0.10 to 0.25 A cm $^{-2}$ but then increases at 1.00 A cm $^{-2}$. We attribute this phenomenon to the increasing mass transport losses at higher current densities because the occurrence of a second semiarc at 0.25 A cm $^{-2}$ can be clearly observed. Presumably, the superposition of the arcs increases until at 1.00 A cm $^{-2}$, the arcs can no longer be distinguished.

3.1.2. Component Regeneration. To investigate the effects of the different cell components on performance loss and degradation, a series of experiments involving stepwise regeneration of the components were conducted in a 4 cm² active area PEMWE single cell. The starting points are the degraded components of cell 6 measured within the stack. As the experiments progressed, an increasing number of cell components were regenerated, as shown in Table 1.

3. As mentioned above, the degraded performance (step 1) was corrected to correspond to a 120- μ m-thick membrane, resulting in the red curve in Figure 3, which is the baseline for the recovery process. In the first regeneration step, the degraded CCM was replaced with a pristine CCM, and the change in the performance was measured, resulting in the orange polarization curve labeled with 2 in Figure 3 a,b.

The performance clearly has increased significantly, although the other components have remained unchanged. For the subsequent experiments, the Ti components were regenerated by removing the TiO_x , starting with the mesh through the PTL to the BPP. For every step, a slight improvement in

performance can be achieved but with a weaker impact than that for the CCM. The dark blue curve labeled with 5 shows the performance of the fully regenerated single cell. For comparison, a reference measurement was conducted with pristine components displayed in green. It is clearly observed that the performance was fully restored. The differences between the pristine cell and the fully regenerated cell are not significant and are due to the experimental errors.

For each regeneration step, electrochemical impedance spectroscopy was conducted. The results at 0.5 A cm⁻² are provided in Figure 3c,d. The red curve labeled with 1 corresponds to the degraded cell components showing high ohmic (HFR) and high overall resistances represented by the first and second intersections, respectively. Replacement of the degraded CCM with a pristine CCM leads to a large decrease in the resistance, as shown by the orange curve in Figure 3d, which is in good agreement with the polarization curves. The subsequent regeneration steps in Figure 3d show a reduction in the HFR because the curves and therefore the intersections are shifted to the left. The widths of the arcs stayed in the same order of magnitude differ by a maximum of approximately 12 $m\Omega cm^2$. This finding indicates that the polishing and cleaning processes had no effect on the properties of the component other than improving the contact resistance by removing the oxide layers on the surfaces. After the CCM, the degradation of PTLs has a major effect on performance loss. The slightly wider arc after the regeneration of the BPP, compared with the previous step, can most likely be attributed to small deviations in the assembly of the single cell. The reference performance represented by the green curve labeled with R in Figure 3b,d could almost be reached by recovering the components. The improvement in voltage at 0.5 A cm⁻² for each component is plotted in Figure 4.

For 0.25 A cm⁻² and 1.0 A cm⁻², the same behavior can be observed, as plotted in SI Figure S4, as well as for the second stack position in SI Figure S5.

3.2. Degradation and Morphology Analysis. A series of different physical ex-situ methods were used to investigate the underlying degradation phenomena, with a major focus on the CCM, as it had the greatest impact on performance loss.

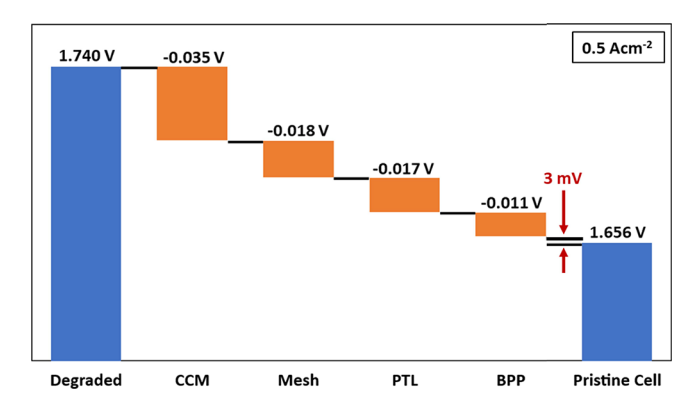
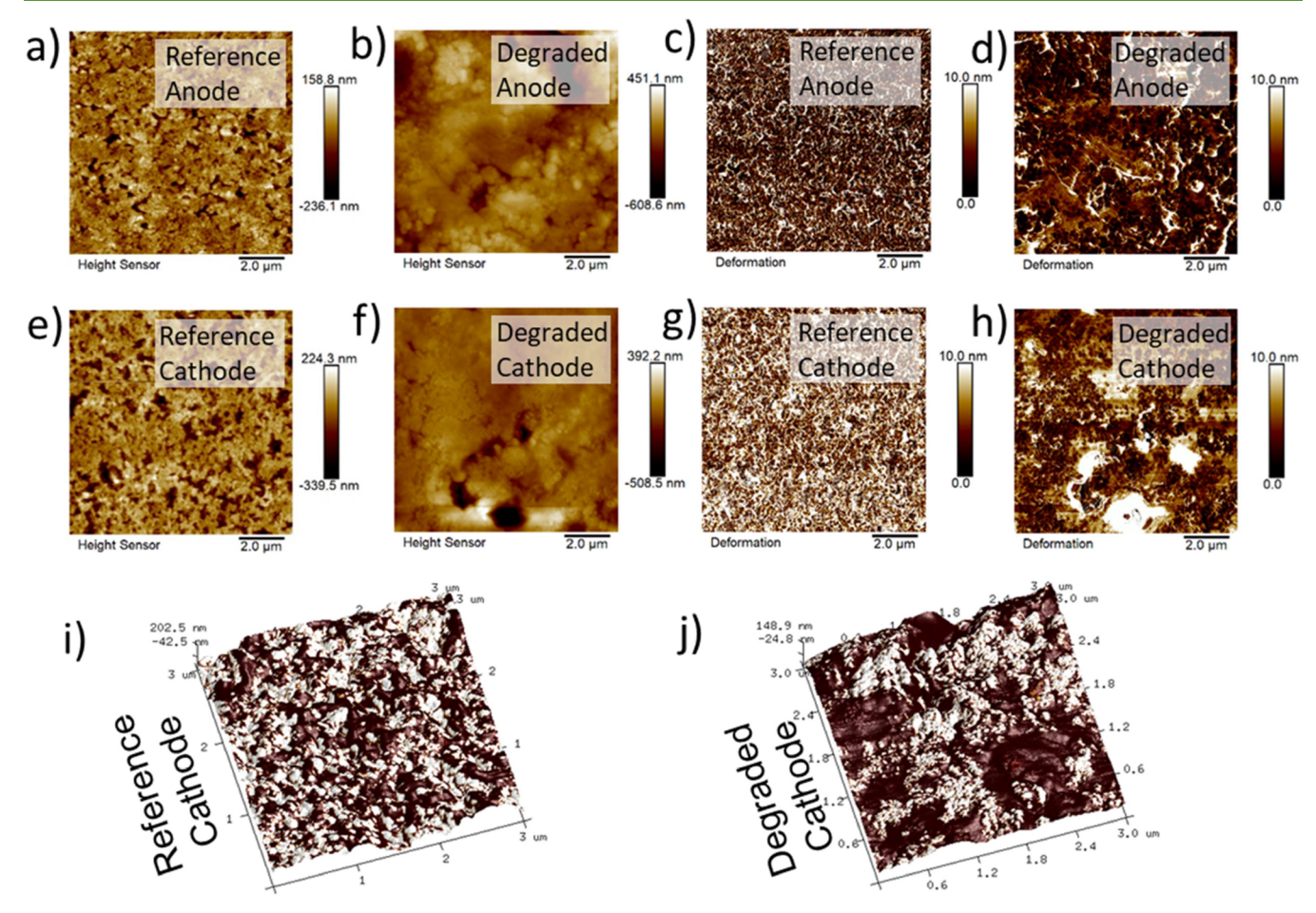


Figure 4. Progression of the improvement in the voltage at 0.5 Acm⁻². The left blue bar shows the voltage of the degraded cell (corrected according to Section 2.2), and the right blue bar shows the voltage of the pristine cell. The orange bars between correspond to the improvements in the voltage for the specific component.

Figures 5 and 6 present the results of the AFM measurements of the CCM anode and cathode side performed with

conductive AFM in the PF-TUNA mode using NCH-Pt AFM tips and the results of DCUBE-TUNA measurements showing the current at 3 V of BPP measured with DDESP tips (other bias and components in SI S6–S9). For the CCM, a reduction in the porosity is particularly noticeable in Figure 5b,f. The ionomer is more deformable than the catalyst and shows no electronic conductivity in AFM measurements, as reported in previous work.⁴³

The nanomechanical properties are evaluated simultaneously, revealing a homogeneous distribution for the reference in Figure 5c,g. However, the formation of larger ionomer areas on the surface is evident in Figure 5d,h. ^{20,26} Additionally, the ionomer agglomerations can be verified via the correlation between the deformation and conductivity properties, as shown in SI Figure S10. This finding is also in good agreement with the nanoelectronic properties. Figure 5i,j show a comparison of the electronic conductivity superimposed on the plotted 3D height between the pristine cathode catalyst layer (CCL, Figure 5i, which shows good performance, and the operated CCL (Figure 5j). The electronic conductive areas are homogeneous over the measured surface in the pristine CCL,



Electronic conductivity superposed on 3D-height data

Figure 5. Nanomechanical and nanoelectrical AFM measurements. (a) Surface structure of pristine reference anode catalyst layer. (b) Surface structure of degraded anode catalyst layer. (c) Deformation analysis of the anodic reference. (d) Ionomer (bright) distribution shown as measured deformation data for the degraded anode. The catalyst is shown in brown. (e) Surface structure of pristine reference cathode catalyst layer. (f) Surface structure of degraded cathode catalyst layer. (g) Deformation analysis of the cathodic reference. (h) Ionomer (bright) distribution shown as measured deformation data for the degraded cathode. The catalyst is shown in brown. (i) Electronic conductivity distribution of the pristine reference cathode catalyst layer surface. (j) Electronic conductivity distribution of the degraded cathode catalyst layer surface.

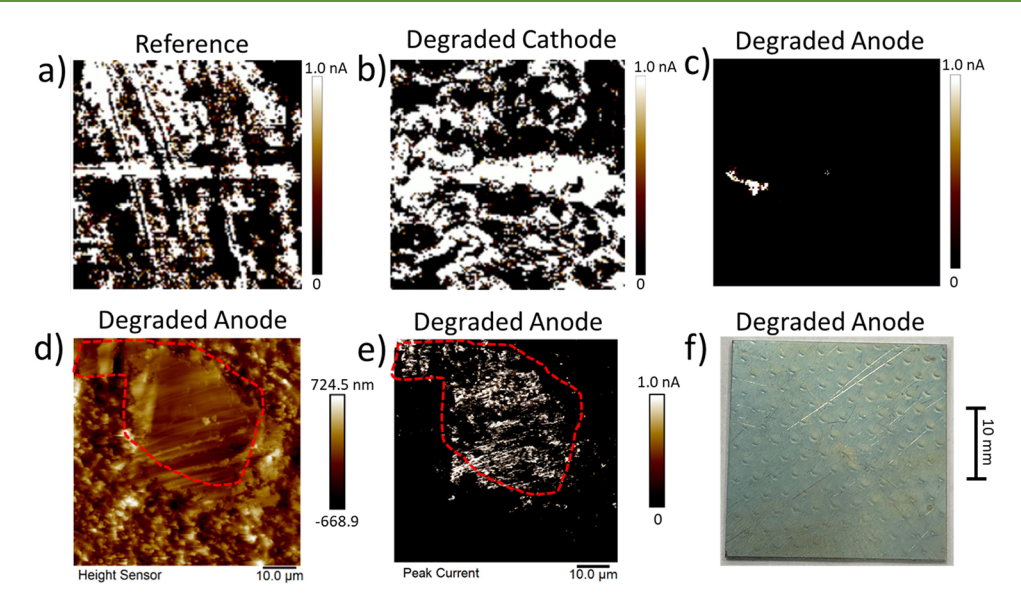


Figure 6. AFM measurements (a) pristine reference BPP showing the electronic conductive structure at 3 V. (b) Operated cathode BPP showing the electronic conductive structure at 3 V. (c) Operated anode BPP showing the electronic conductive structure at 3 V. (d) Large area measurement showing the height structure of one contact point of the mesh. (e) Electronic conductivity data measured simultaneously with the height measurements in (d). (f) Photograph of the BPP showing the oxide layer and the contact points with the mesh.

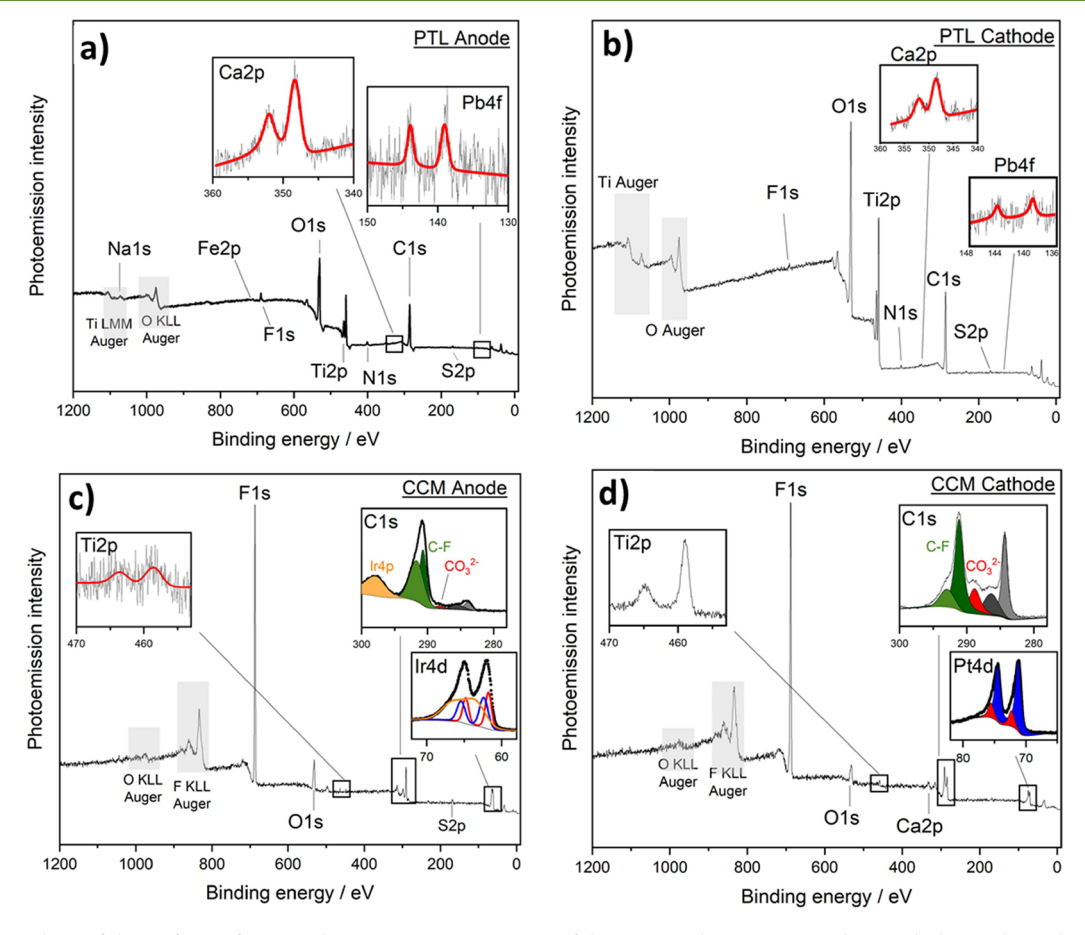


Figure 7. XPS analysis of the surfaces of PTL and CCM. Overview spectra of the Ti PTL show unexpected Ca and Pb signals on the (a) anode side and (b) cathode side, and the CCM spectra show traces of Ti and carbonate components in the C 1s signal on the (c) anode side and (d) cathode side.

whereas the agglomeration of nonelectronically and electronically conductive surfaces can be clearly observed on the operated sample surface in Figure 5j; this may be due to

various mechanisms described mainly for a proton exchange membrane fuel cell (PEMFC) but that are also applicable for PEMWE, such as Ostwald ripening, catalyst dissolution and

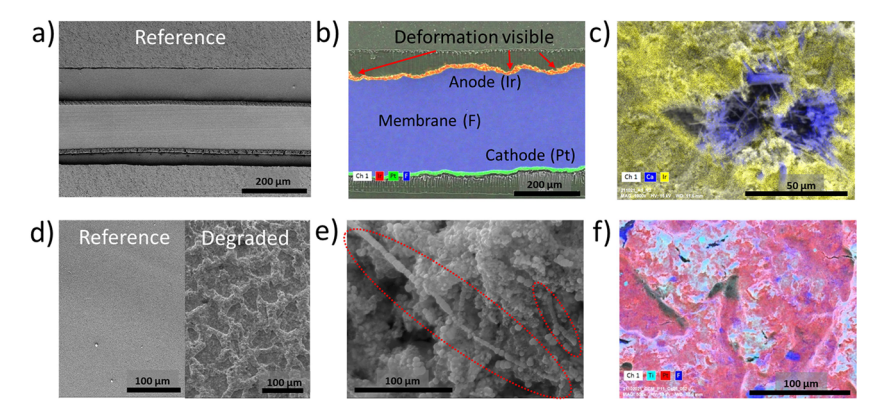


Figure 8. SEM and EDX measurements of the degraded CCM. (a) Cross-section of the reference CCM. (b) Microtome cross-section superimposed with EDX-mapping data showing the catalyst layers and membrane due to Ir, F and Pt. (c) Surface measurement of the anode showing that calcium (blue) penetrated the catalyst layer. (d) Surface comparison of the reference and degraded CCM. (e) Iridium agglomerates at the anode surface, building an "Ir chain." (f) EDX mapping of the cathode surface showing ionomer agglomeration (F in blue) and Ti deposition (cyan).

redeposition or catalyst detachment, which can occur either individually or simultaneously. ^{11,16,26} Due to this agglomeration at the surface, a reduced contact at the triple phase boundary can be assumed, resulting in a significant reduction in performance. In addition, a reduced porosity due to ionomer agglomeration at the surface may lead to mass transport problems.

In addition, AFM analyses were conducted to investigate the surface conductivity of the metallic components. The dark areas correlate with low conductivity up to complete nonconductivity shown in black. Lighter color indicates greater conductivity. The reduced conductivity of metallic components can be attributed to the formation of oxide layers during operation. For BPP, a clear oxidation of the surface of the anode can be observed, as shown in the photograph presented in Figure 6f, and also by the reduced conductivity observed in Figure 6c. The cathode side (Figure 6b) showed a similar conductivity as the pristine reference sample (Figure 6a). The regenerated sample of the anode again showed the same conductivity as the pristine reference sample, so that it can be assumed that the reduction in the conductivity was due to oxidation of the surface and the formation of a high-resistance interlayer of TiOx. Interestingly, the measurement of a significantly larger surface area revealed that the areas that were not in contact with the mesh were oxidized and showed no conductivity in the measured voltage range up to 3 V. By contrast, the areas in direct contact with the mesh retained their conductivity, as indicated in Figure 6d,e. This observation is in good agreement with the previously performed EIS analyses, which show only a weak impact of the BPPs on the ohmic resistances. A reduced conductivity at the anode side and nearly unchanged conductivity at the cathode were also observed for the PTL.

Figure 7 shows an overview of the photoemission spectra (XPS) of a PTL and a CCM, indicating the observed elements and presenting selected detailed spectra in the insets. The presence of small amounts of Ca deposits on the PTL is revealed together with the expected signals of Ti and oxygen in the PTL material and its native oxide layer. Oxygen is more pronounced on the anode side in Figure 7a, which is in good agreement with the higher oxidation rates shown for the BPP in Figure 6. Ca may have been introduced into the system via the cleaning water during the manufacturing of the

components or due to a malfunctioning water purifying system of the PEMWE. Other contaminants are C, F, and S as traces of membrane and electrode ionomers. Iron is most likely due to deposited traces from piping and other parts of the balanceof-plant (BoP). Sodium is a commonly abundant trace element in water circuits and can accumulate on surfaces. Most interestingly, a small amount of Pb could be unmistakably identified at several positions (and other Ti components, see SI Figure S11); its absence in the results obtained by other less surface-sensitive analysis methods confirms its origin as a surface deposit. It is, however, less pronounced on the operated components than on the new components. The origin of the Pb could not be determined with certainty and can only be speculated, but as it was found on the pristine components and unpurified cleaning water was used, therefore it may also have been introduced via the cleaning water. The analysis of the CCM in Figure 7c,d revealed the expected elements, such as C, F, and Pt/Ir, as well as traces of Ti. Presumably, the Ti originates from the uncoated Ti components used on both the anode and cathode sides. Particularly for the anodic Ti parts that are in direct contact with the acid polymer, Ti dissolution may occur during oxygen evolution. 44 Because uncoated Ti-PTLs are used on the cathode side, the Ti deposition on that side is caused by either Ti migration through the membrane from the anode to the cathode, direct deposition due to the Ti-PTLs or a combination of both. 13 A detailed analysis of the carbon 1 s signal, as depicted in the insets in Figure 7c,d, revealed a signal at ~289 eV, which is typically attributed to solid carbonates. However, the calculated abundances for the assumed carbonates are significantly higher than those for Ca only, so that it is quite likely that a mixture of different surface carbonates is presented. The CCM itself even accounts for ~5 at% of the assumed carbonate signal, but in contrast to the Ti components, no Ca could be detected by XPS. A similar possible signal of carboxylates in the mixture of catalyst carrier and ionomer cannot be distinguished in the present materials.

Figure 8 presents the results of the SEM and EDX analyses of the aged CCM. A comparison of the cross sections of the pristine reference CCM in Figure 8a and of the aged CCM in Figure 8b reveals one conspicuous feature, namely creeping of the membrane, most likely because the PTL is pressed against the catalyst layers. Although this effect is visible for the entire

surface shown in Figure 8d, it does not necessarily reflect a degradation phenomenon that negatively affects performance. No abnormalities were detected in the membrane itself. On the anode side, calcium deposits were found (Figure 8c), some of which have assumed crystalline structures such as aragonite and CaCO₃. In these areas, the functionality of the layer is not given. Penetration of the membrane by the crystalline structures is also possible but was not observed in the crosssection. Additionally, other CaCO₃ structures covering the catalyst layer were found, which prevent normal operation in these areas. Furthermore, calcium does not appear to be present on the surface or only has a very small surface distribution, because it could not be detected even by XPS. The CCL showed clear signs of degradation effects due to operation (Figure 8e,f). Agglomeration of Ir was observed, even the formation of long chains, visible in the red circled area of Figure 8e. Liu et al. reported similar changes in morphology and hypothesized that dissolution, agglomeration, and particle growth due to coalescence/redeposition are the driving factors.²⁶ Furthermore, they assume that different operation conditions have different effects on the morphology of the catalyst. Consequently, unfavorable changes in the morphology can be reduced or prevented by optimized operating profiles. In Figure 8f, larger areas with high fluorine contents were observed on the cathode side with EDX mapping, together with Ti deposits caused by the uncoated Ti components. 13,44 A direct comparison of the anode side CCM using SEM/EDX is shown in SI Figure S12.

X-ray diffraction was used to investigate the structure of the Ca detected by EDX/SEM. The X-ray diffractogram of the CCM is plotted in SI Figure S13. Crystalline Ir was identified on the anode side of the CCM. The sharp Ir peak profile in the anodic CCM indicates its high crystallinity and large crystallite size. Apparently, no other crystalline phase was observed on the anode side; thus, calcium was not detected. The fact that no evidence of calcium was found by XRD would indicate that it has an amorphous structure, but even if comparable large calcium agglomerations were observed by EDX/SEM, the overall surface distribution of calcium was so small that it is possible that its signal was below the detection limit and could not be resolved in the vicinity of the pronounced Ir signal. Therefore, it could not be determined whether calcium was present in crystalline or amorphous structures. In principle, the formation of carbonates can result in a decreased contact area and therefore increased contact resistance of the cells, which was detected in this study.⁴⁶

4. CONCLUSIONS

In this study, a novel approach involving the successive replacement of aged components was used to analyze the degradation phenomena of a proton exchange membrane water electrolyzer (PEMWE) stack. This approach was used to simplify the analysis of stack components and perform it in a time-efficient and reliable manner. For this approach, the stack components were prepared for use in a 4 cm² single cell. The catalyst coated membrane (CCM) was identified as the component with the greatest impact on degradation, followed by the Ti porous transport layer (PTL).

Several degradation phenomena for the CCM were detected, such as agglomeration of the Ir catalyst, presumably caused by unfavorable operation conditions.²⁶ Moreover, on the cathode side, ionomer agglomeration^{20,26} as well as titanium deposits were found, the latter caused by direct contact with the

titanium PTLs. ¹³ In addition, calcium deposits were observed due to insufficient water quality either during initial cleaning processes of the Ti components or during operation. The main degradation phenomenon of the PTL and the bipolar plate (BPP) was the formation of oxide layers, which led to an increase in the high-frequency resistance (HFR). This phenomenon was much more pronounced on the anode side. Therefore, by regenerating the Ti components and using a pristine CCM, the performance of the cell was almost fully restored. This particular result is of interest because it demonstrates how certain stack components can be reused to make the technology more sustainable and reduce costs.

In conclusion, our novel approach in combination with electrochemical analysis and various physical ex situ methods represents an efficient method for the analysis and investigation of the components of a PEMWE stack. The analysis can be performed using standard laboratory equipment and breaking down from the stack to a single cell. Current studies usually conduct such investigations without examining the impact of separate components on performance and degradation. Therefore, this method improves the development and optimization of, for example new components or new coatings by determining the impact of the components separately.

ASSOCIATED CONTENT

Supporting Information

The Supporting Information is available free of charge at https://pubs.acs.org/doi/10.1021/acssuschemeng.4c07358.

Electrochemical measurements; Ohmic resistances determined by EIS; voltage improvement for each recovery step; atomic force microscope analysis; scanning electron microscopy and energy dispersive X-ray spectroscopy analysis; X-ray photoelectron spectroscopy analysis; and X-ray diffraction analysis (PDF)

AUTHOR INFORMATION

Corresponding Author

Aldo Saul Gago — Institute of Engineering Thermodynamics, German Aerospace Center (DLR), 70569 Stuttgart, Germany; orcid.org/0000-0001-7000-171X; Email: aldo.gago@dlr.de

Authors

Benjamin Kimmel – Institute of Engineering Thermodynamics, German Aerospace Center (DLR), 70569 Stuttgart, Germany

Tobias Morawietz — Institute of Engineering Thermodynamics, German Aerospace Center (DLR), 70569 Stuttgart, Germany; Faculty of Science, Energy and Building Services, Esslingen University of Applied Sciences, 73728 Esslingen am Neckar, Germany

Indro Biswas – Institute of Engineering Thermodynamics, German Aerospace Center (DLR), 70569 Stuttgart, Germany

Noriko Sata – Institute of Engineering Thermodynamics, German Aerospace Center (DLR), 70569 Stuttgart, Germany

Pawel Gazdzicki – Institute of Engineering Thermodynamics, German Aerospace Center (DLR), 70569 Stuttgart, Germany Kaspar Andreas Friedrich — Institute of Engineering Thermodynamics, German Aerospace Center (DLR), 70569 Stuttgart, Germany; Institute for Building Energetics, Thermotechnology and Energy Storage, University of Stuttgart, 70174 Stuttgart, Germany; orcid.org/0000-0002-2968-5029

Complete contact information is available at: https://pubs.acs.org/10.1021/acssuschemeng.4c07358

Funding

The research reported here was funded by the Federal Ministry of Education and Research's (BMBF) Hypos-Initiative under Grant No. 03ZZ0742A (ElyKon).

Notes

The authors declare no competing financial interest.

REFERENCES

- (1) Barnhart, C. J.; et al. The energetic implications of curtailing versus storing solar- and wind-generated electricity. *Energy Environ. Sci.* **2013**, *6* (10), 2804.
- (2) Smolinka, T.; Ojong, E. T.; Garche, J. Hydrogen Production from Renewable Energies—Electrolyzer Technologies. *Electrochemical Energy Storage for Renewable Sources and Grid Balancing*. **2015**, 103.
- (3) Lettenmeier, P.; et al. Coated Stainless Steel Bipolar Plates for Proton Exchange Membrane Electrolyzers. *J. Electrochem. Soc.* **2016**, 163 (11), F3119–F3124.
- (4) Kang, Z.; et al. Performance Modeling and Current Mapping of Proton Exchange Membrane Electrolyzer Cells with Novel Thin/Tunable Liquid/Gas Diffusion Layers. *Electrochim. Acta* **2017**, 255, 405–416.
- (5) Kang, Z., Investigation of Pore Shape Effects of Novel Thin LGDLs for High-Efficiency Hydrogen/Oxygen Generation and Energy Storage. In 15th International Energy Conversion Engineering Conference, 2017.
- (6) Lettenmeier, P.; et al. Towards developing a backing layer for proton exchange membrane electrolyzers. *J. Power Sources* **2016**, *311*, 153–158.
- (7) Shirvanian, P.; van Berkel, F. Novel components in Proton Exchange Membrane (PEM) Water Electrolyzers (PEMWE): Status, challenges and future needs. A mini review. *Electrochem. Commun.* **2020**, *114*, No. 106704.
- (8) Lee, J. K.; et al. Spatially graded porous transport layers for gas evolving electrochemical energy conversion: High performance polymer electrolyte membrane electrolyzers. *Energy Conversion and Management* **2020**, 226, No. 113545.
- (9) Liu, J.; et al. Efficient and Stable Proton Exchange Membrane Water Electrolysis Enabled by Stress Optimization. *ACS Cent Sci.* **2024**, *10* (4), 852–859.
- (10) Stiber, S.; et al. Porous Transport Layers for Proton Exchange Membrane Electrolysis Under Extreme Conditions of Current Density, Temperature, and Pressure. *Adv. Energy Mater.* **2021**, *11* (33), No. 2100630.
- (11) Rakousky, C.; et al. Polymer electrolyte membrane water electrolysis: Restraining degradation in the presence of fluctuating power. *J. Power Sources* **2017**, 342, 38–47.
- (12) Alia, S. M. Current research in low temperature proton exchange membrane-based electrolysis and a necessary shift in focus. *Current Opinion in Chemical Engineering* **2021**, 33, No. 100703.
- (13) Rakousky, C.; et al. An analysis of degradation phenomena in polymer electrolyte membrane water electrolysis. *J. Power Sources* **2016**, 326, 120–128.
- (14) Rakousky, C.; et al. The stability challenge on the pathway to high-current-density polymer electrolyte membrane water electrolyzers. *Electrochim. Acta* **2018**, 278, 324–331.
- (15) Siracusano, S.; et al. Degradation issues of PEM electrolysis MEAs. Renewable Energy 2018, 123, 52–57.
- (16) Spori, C.; et al. The Stability Challenges of Oxygen Evolving Catalysts: Towards a Common Fundamental Understanding and

- Mitigation of Catalyst Degradation. Angew. Chem., Int. Ed. Engl. 2017, 56 (22), 5994–6021.
- (17) Yu, H.; et al. Microscopic insights on the degradation of a PEM water electrolyzer with ultra-low catalyst loading. *Applied Catalysis B: Environmental* **2020**, 260, No. 118194.
- (18) Weiß, A.; et al. Impact of Intermittent Operation on Lifetime and Performance of a PEM Water Electrolyzer. *J. Electrochem. Soc.* **2019**, *166* (8), F487–F497.
- (19) Alia, S. M.; Stariha, S.; Borup, R. L. Electrolyzer Durability at Low Catalyst Loading and with Dynamic Operation. *J. Electrochem. Soc.* **2019**, *166* (15), F1164–F1172.
- (20) Morawietz, T.; et al. High-Resolution Analysis of Ionomer Loss in Catalytic Layers after Operation. *J. Electrochem. Soc.* **2018**, *165* (6), F3139–F3147.
- (21) Reier, T.; Oezaslan, M.; Strasser, P. Electrocatalytic Oxygen Evolution Reaction (OER) on Ru, Ir, and Pt Catalysts: A Comparative Study of Nanoparticles and Bulk Materials. *ACS Catal.* **2012**, *2* (8), 1765–1772.
- (22) Alia, S. M.; et al. Activity and Durability of Iridium Nanoparticles in the Oxygen Evolution Reaction. *J. Electrochem. Soc.* **2016**, *163* (11), F3105–F3112.
- (23) Alia, S. M.; Anderson, G. C. Iridium Oxygen Evolution Activity and Durability Baselines in Rotating Disk Electrode Half-Cells. *J. Electrochem. Soc.* **2019**, *166* (4), F282–F294.
- (24) Zeng, Y.; et al. A cost-effective nanoporous ultrathin film electrode based on nanoporous gold/IrO2 composite for proton exchange membrane water electrolysis. *J. Power Sources* **2017**, 342, 947–955.
- (25) Jovanovic, P.; et al. Electrochemical Dissolution of Iridium and Iridium Oxide Particles in Acidic Media: Transmission Electron Microscopy, Electrochemical Flow Cell Coupled to Inductively Coupled Plasma Mass Spectrometry, and X-ray Absorption Spectroscopy Study. *J. Am. Chem. Soc.* **2017**, *139* (36), 12837–12846.
- (26) Liu, C.; et al. Degradation Effects at the Porous Transport Layer/Catalyst Layer Interface in Polymer Electrolyte Membrane Water Electrolyzer. *J. Electrochem. Soc.* **2023**, 170 (3), No. 034508.
- (27) Siracusano, S.; et al. Enhanced performance and durability of low catalyst loading PEM water electrolyser based on a short-side chain perfluorosulfonic ionomer. *Applied Energy* **2017**, *192*, 477–489.
- (28) Grigoriev, S. A.; et al. Failure of PEM water electrolysis cells: Case study involving anode dissolution and membrane thinning. *Int. J. Hydrogen Energy* **2014**, 39 (35), 20440–20446.
- (29) Sun, S.; et al. Investigations on degradation of the long-term proton exchange membrane water electrolysis stack. *J. Power Sources* **2014**, 267, 515–520.
- (30) Suermann, M.; et al. Femtosecond laser-induced surface structuring of the porous transport layers in proton exchange membrane water electrolysis. *Journal of Materials Chemistry A* **2020**, 8 (9), 4898–4910.
- (31) Liu, C.; et al. Exploring the Interface of Skin-Layered Titanium Fibers for Electrochemical Water Splitting. *Adv. Energy Mater.* **2021**, *11* (8), No. 2002926.
- (32) Stiber, S.; et al. Long-Term Operation of Nb-Coated Stainless Steel Bipolar Plates for Proton Exchange Membrane Water Electrolyzers. Advanced Energy and Sustainability Research 2022, 3 (8), No. 2200024.
- (33) Lettenmeier, P.; et al. Low-Cost and Durable Bipolar Plates for Proton Exchange Membrane Electrolyzers. *Sci. Rep* **2017**, *7*, 44035.
- (34) Feng, Q.; et al. A review of proton exchange membrane water electrolysis on degradation mechanisms and mitigation strategies. *J. Power Sources* **2017**, *366*, 33–55.
- (35) KG, Z.-E. G. C. Zahner-Elektrik GmbH & Co. KG. 2024 [accessed 22.08.2024]; Available from: https://zahner.de/.
- (36) T, M., EU harmonised polarisation curve test method for low-temperature water electrolysis. European Commission, Editor. 2018
- (37) Corti, H. R. Polymer electrolytes for low and high temperature PEM electrolyzers. Current Opinion. Electrochemistry 2022, 36, No. 101109.

- (38) Bernt, M.; et al. Analysis of Gas Permeation Phenomena in a PEM Water Electrolyzer Operated at High Pressure and High Current Density. *J. Electrochem. Soc.* **2020**, *167* (12), 124502.
- (39) Martin, A.; et al. Hydrogen Crossover in PEM Water Electrolysis at Current Densities up to 10 A cm-2. *J. Electrochem. Soc.* **2022**, *169* (9), No. 094507.
- (40) Rozain, C.; et al. Influence of iridium oxide loadings on the performance of PEM water electrolysis cells: Part I—Pure IrO 2 -based anodes. *Applied Catalysis B: Environmental* **2016**, *182*, 153–160.
- (41) Hesse, R.; Chassé, T.; Szargan, R. Peak shape analysis of core level photoelectron spectra using UNIFIT for WINDOWS. *Fresenius' J. Anal. Chem.* **1999**, 365 (1–3), 48–54.
- (42) Lettenmeier, P.; et al. Comprehensive investigation of novel pore-graded gas diffusion layers for high-performance and cost-effective proton exchange membrane electrolyzers. *Energy Environ. Sci.* **2017**, *10* (12), 2521–2533.
- (43) Lagarteira, T.; et al. Highly active screen-printed Ir Ti4O7 anodes for proton exchange membrane electrolyzers. *Int. J. Hydrogen Energy* **2018**, *43* (35), 16824–16833.
- (44) Cherevko, S.; et al. Stability of nanostructured iridium oxide electrocatalysts during oxygen evolution reaction in acidic environment. *Electrochem. Commun.* **2014**, *48*, 81–85.
- (45) Ševčík, R.; Šašek, P.; Viani, A. Physical and nanomechanical properties of the synthetic anhydrous crystalline CaCO3 polymorphs: vaterite, aragonite and calcite. *J. Mater. Sci.* **2018**, *53* (6), 4022–4033.
- (46) Grimmig, R.; et al. Operating an ozone-evolving PEM electrolyser in tap water: A case study of water and ion transport. Sep. Purif. Technol. 2022, 292, No. 121063.